JOURNAL OF PROPULSION AND POWER
Vol. 21, No. 1, January–February 2005

Elastic Scattering of Ions in Electrostatic Thruster Plumes

Ioannis G. Mikellides* and Ira Katz†
Jet Propulsion Laboratory, California Institute of Technology, Pasadena, California 91109
and
Robert A. Kuharski‡ and Myron J. Mandell‡
Science Applications International Corporation, San Diego, California 92121

It is postulated that the ion population and energy in most ion and Hall-Effect thruster plumes, at angles beyond the main beam divergence, is largely determined by the elastic scattering of high-energy ions by neutral atoms. A theoretical model of the scattered ion density and energy is presented. The model accounts for the presence of a main ion beam emanating from the thruster and neutral atoms from the ambient and thruster-induced environment. The treatment of elastic scattering incorporates angle-dependent differential cross sections that are computed classically. Results from the model are compared with ion flux and energy measurements taken by a retarding potential analyzer as a function of angle from the thruster's axis of symmetry. The good agreement between model results and measurements for ion energy and flux suggests that the determination of the differential cross section using classical formulations is adequate for the high-energy ions associated with electrostatic propulsion plumes. But the comparisons also emphasize the importance of accurate models of the neutral particle densities in these plumes.

Nomenclature

A = area of thruster acceleration channel, m^2
E = impact energy associated with the scattering event, eV
F = ion particle flux, particles/m^2 s
Fr = radial component of ion flux vector, particles/m^2 s
Fz = axial component of ion flux vector, particles/m^2 s
f = multiple ionization flux fraction
I = differential cross section, m^2/sr
J = current, A
M = reduced mass, kg
m = particle mass, kg
$\dot{m}_i$ = ion mass flow rate, kg/s
N = number of scattered particles
n = ion particle density, particles/m^3
n_0 = neutral particle density, particles/m^3
n_∞ = reference ion particle density, particles/m^3
P = vacuum chamber pressure, torr
p = plasma pressure, Pa
q = charge, C
R = distance between colliding particles, m
R_m = distance of nearest approach between colliding particles, m
r = radial coordinate in polar system, m
S = surface area penetrated by scattered ions, m^2
t = time, s
$\boldsymbol{U}$ = relative velocity between colliding particles, m/s
$\boldsymbol{u}$ = single particle velocity, m/s
u_r = radial component of ion velocity, m/s
u_z = axial component of ion velocity, m/s
V = collision interaction potential energy, eV
Z = charge state
z = axial coordinate in polar system, m
α = energy coefficient in repulsive part of interaction potential function, eV
β = impact parameter, m
$\in$ = energy of ion after scattering event, J
ζ = power coefficient in repulsive part of interaction potential function
Θ = deflection angle, rad
θ = scattering angle in center-of-mass (CM) frame, rad
ϑ = scattering angle in laboratory frame, rad
λ = characteristic length coefficient in repulsive part of interaction potential function, m
ρ = position vector between scattering point and field node, m
σ = collision cross section area, m^2
υ = integration volume, m^3
Φ = electric potential, V
ϕ = angle in polar coordinate system, rad
ψ = plume half angle, rad
Ω = solid angle, sr

Subscripts

b = value associated with main beam ion
c = center of mass
e = electron
eff = effective value
L = laboratory frame
ε = value associated with elastically scattered ion

Superscripts

f = value at field node
s = value at scattering point
sf = value associated with scattering event between scattering point s and field node f

Presented as Paper 2001-3355 at the AIAA/ASME/SAE/ASEE 37th Joint Propulsion Conference, Salt Lake City, UT, 8–11 July 2001 and as Paper 2003-4871 at the AIAA/ASME/SAE/ASEE 39th Joint Propulsion Conference, Huntsville, AL, 20–23 July 2003; received 7 September 2003; revision received 24 May 2004; accepted for publication 19 May 2004.

*Senior Scientist, Advanced Propulsion Technology Group, Thermal and Propulsion Engineering Section, 4800 Oak Grove Drive; currently Senior Staff Scientist, Science Applications International Corporation, Defense Technology Group, 10260 Campus Point Drive, San Diego, CA 92121. Member AIAA.

†Supervisor, Advanced Propulsion Technology Group, Thermal and Propulsion Engineering Section, 4800 Oak Grove Drive. Senior Member AIAA.

‡Senior Staff Scientist, Defense Technology Group, 10260 Campus Point Drive, Mail Stop A1. Senior Member AIAA.

Introduction

IONS in the plumes of ion propulsion systems (IPSs) and Hall-effect thrusters (HETs) have usually been associated with two main ion sources. The first is ionization of neutral propellant in the thruster chamber. These "main-beam" ions dominate the population of heavy ionized species within approximately 45 deg of the thruster axis of symmetry and are highly energetic because they are accelerated directly by the applied electric field. The second source of ions is charge exchange (CEX) between main-beam ions and neutral gas particles. The neutral gas is due to unionized particles leaving the thruster and the neutralizer (hollow cathode), as well as background neutrals that are present in the vacuum chamber if the thruster is operating in the laboratory. CEX reactions are commonly associated with inelastic collision processes that produce low-energy ions with less than about 15% of the main-beam ion energy. Due to their low energy, CEX ions are expelled from the main plume by electric forces directed radially outward and thus dominate the plasma at large plume angles (>70 deg). CEX ions may also be attracted back to negatively-biased spacecraft and propulsion-system components, leading to unfavorable interactions. One primary example of the adverse effects of CEX ions is erosion of the acceleration grid in an IPS. Past empirical and theoretical work has focused mainly on these two plume components, namely main-beam and CEX ions.[1–4]

CEX reactions have a relatively large total collision cross section. For example, the xenon CEX cross section is approximately 55 Å^2 for 300-eV single ions and remains fairly unchanged at higher energies.[5] Such large proximities within which an ion and neutral can exchange charge leave the new ion with relatively low kinetic energy, less than 50 eV for 300-eV main-beam xenon ions. However, ions can also elastically scatter to high angles while retaining a sensible fraction of their initial energy. Because they may be scattered to angles larger than the typical main-beam plume divergence angle (usually <45 deg), plume ions with higher energies may lead to serious compications associated with the integration of IPSs and/or HETs onboard spacecraft. In the laboratory the contribution of elastically scattered ions is enhanced by the higher neutral concentrations that exist as a result of the chamber background gas. A predictive capability is essential in these cases because it can aid in the extraction of terrestrial facility effects that can distort plume measurements.

Evidence of High-Energy Ions at Large Angles in a Hall-Effect Thruster Plume

Experiments with a 4-kW class Hall-effect thruster (BPT-4000; Fig. 1) provided evidence of the existence of high-energy ions in the thruster's plume. The data presented here were obtained when the HET was operated at a discharge power and voltage of 3 kW and 300 V, respectively. Plume measurements were taken using fully exposed flux probes ("uncollimated") to assess the nondirectional ion flux and probes inside graphite collimators ("collimated").[6] Figure 2 shows ion-energy spectra measured at different plume angles with respect to the thruster axis of symmetry using a collimated retarding potential analyzer (RPA). The angle-independent high-energy peak at 280 eV associated with the main beam is clearly evident. Conversely, the characteristic small-amplitude CEX ion peaks are observed at the lowest energy values of the collimated spectra. The CEX peak is more evident at approximately 10 eV in the uncollimated data of Fig. 3.

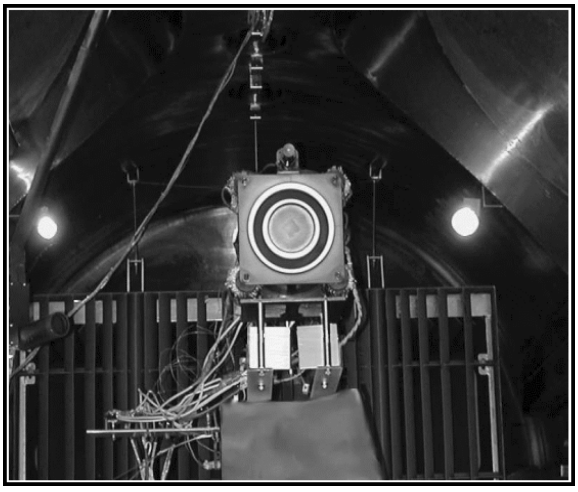

Fig. 1 Front view of the Hall-effect engine BPT-4000 in the vacuum chamber.

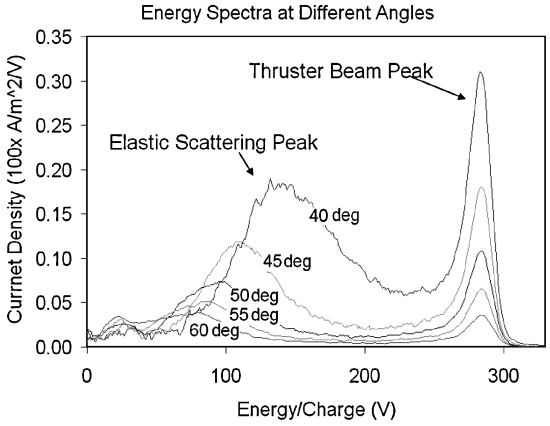

Fig. 2 Collimated RPA measurements at various angles with respect to the BPT-4000 axis of symmetry.

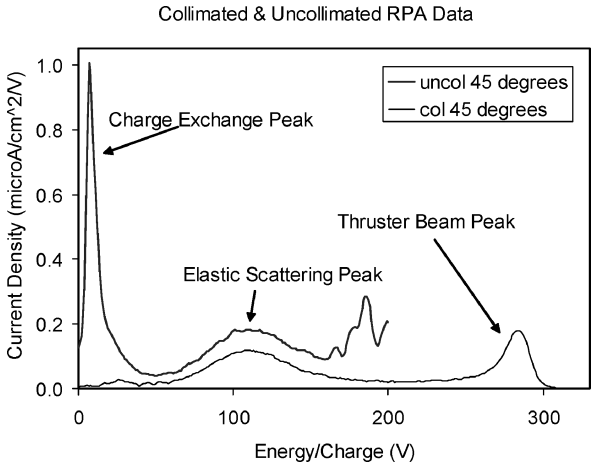

Fig. 3 Comparison between collimated and uncollimated RPA measurements at 45 deg from the BPT-4000 axis of symmetry.

Figure 2 further reveals the existence of secondary current-density peaks with relatively high energies compared to the characteristic charge-exchange peak. For example, at a plume half-angle of $\psi = 40$ deg the energy associated with the second maximum is approximately 150 eV. These observed ion-flux crests show a marked energy dependence on angle. The energy dependence is observed to vary very nearly as $E_L \cos^2\psi$, providing strong evidence that these ions result from elastic scattering of main-beam ions by neutrals. With the introduction of more powerful sources in space flight (such as nuclear) a predictive model of such scattering processes becomes critical. For many high-energy (>5 km/s) robotic missions to the outer planets, IPSs and HET systems are intended to operate at high power levels (>10 kW) for increased specific impulse and thrust. Depending on the applied voltage, main-beam ion energies may range to thousands of eV at propellant flow rates exceeding a few milligrams per second. The enhanced energies and fluxes of elastically scattered ions expected at these higher jet-power levels (where jet power is proportional to the product of the ion flow rate and the square of the ion velocity) can cause more severe damage to surrounding spacecraft structures and diagnostics than their lower-power (<3 kW) counterparts.

Plume Model

Main Beam Ions and Neutral Particles

Although there appears to be general agreement on the physical principles governing the expansion of the main-beam ions, the numerical approaches employed to model them vary. The model presented here employs a Lagrangian fluid algorithm. Other approaches that are based on the "particle-in-cell" (PIC) method[7] have also been used successfully. The fluid algorithm is chosen here in order to eliminate numerical "shot" noise exhibited many times in standard PIC by statistical fluctuations of the discrete N-particle system. Noise in the calculations can be manifested through an increase of the concentration of high-energy beam particles at large angles (>45 deg) and may therefore lead to an unphysical contribution to the population of elastically scattered ions. The fluid algorithm has been applied in the past to model the expansion of main-beam ions in HETs. The model formulation and numerical approach, imposed boundary conditions at the thruster exit, and comparisons with on-orbit and laboratory data have been presented in detail elsewhere.[1,8] The basic approach is repeated here for completeness.

The primary beam of ions exhausted from the thruster is assumed to be a collisionless, singly ionized, quasi-neutral ($n_e = n_i$) plasma expanding under the influence of the (density-gradient) electric field. Therefore, the present beam model does not include the contributions of (ion) gas-dynamic pressure forces to the ion expansion. By comparison to heavy-particle motion, electrons reach dynamic equilibrium at much smaller characteristic times. The electron-inertia term may therefore be neglected in the equation of motion. In the absence of electron–ion collisions and magnetic fields, conservation of momentum for the electrons is expressed by

$$m_e \frac{\mathrm{D}\boldsymbol{u}_e}{\mathrm{D}t} = q_e \nabla \Phi - \frac{\nabla p}{n} = 0 \tag{1}$$

Assuming ideal-gas behavior and isothermal electrons, integration of Eq. (1) leads to the Boltzmann relation, which can be expressed in terms of the electric potential as follows:

$$\Phi(n, T_e) = T_e \ln(n/n_\infty) \tag{2}$$

Equation (2) is sometimes also known as the *barometric potential law*. An effective temperature of 8 eV (Ref. 1) has been used in all HET plume simulations presented here.

Ions are accelerated by the electric field, $\mathrm{E} = -\nabla\Phi$, according to

$$m_i \frac{\mathrm{D}\boldsymbol{u}_b}{\mathrm{D}t} = -q_e \nabla \Phi \tag{3}$$

Because the drift velocity of the ions is much greater than their thermal velocity, the high-velocity ions are modeled as a fluid. The steady-state conservation equations for mass and momentum [given by Eq. (4)] are solved in two-dimensional (R–Z) geometry:

$$\nabla \cdot n\boldsymbol{u}_b = 0, \qquad m_i \boldsymbol{u}_b \cdot \nabla \boldsymbol{u}_b = -\nabla_p / n \tag{4}$$

The numerical algorithm for computing the expansion of the main ion beam is based on a Lagrangian approach. Discrete mass elements are released from the thruster exit and"tracked" using fundamental trajectory kinematics. Assuming that variations in the electric field occur on a much larger time scale than ion transit times, the location of each "macroparticle" at time t is computed. At each successive time interval Δt the density is updated using conservation of mass [Eq. (4), top]. With the updated density, the plasma potential [Eq. (2)] and electric field are recomputed for the next iteration. The iterative process uses a predictor–corrector method and continues until ion trajectories are consistent with the local electric field. In steady state the trajectories and particle locations at different times form a fictitious grid from which particle density and velocity are interpolated onto a fixed grid using the values of the surrounding trajectory grid points.

The prediction of ion expansion from the Hall thruster requires knowledge of the conditions at the exit. In the present effort the exit conditions have been determined based on the thruster operating parameters listed in Table 1. In a Hall thruster both the current density and the ion-velocity vector vary along the exit. The (relative) radial profile of the ion-current density implemented at the exit boundary is shown in Fig. 4 (ρ_{out} denotes the thruster outer radius). The profile is based on integrated values of measurements obtained during laboratory tests of the BPT-4000 (Ref. 9). The radial component of the ion-velocity vector is varied linearly along the thruster exit ranging from -8 to $+8$ km/s at the inner and outer thruster radii, respectively. The choice of the radial-velocity profile is an estimate that is based on velocity measurements taken in the near field of a stationary plasma thruster (SPT-140) (Ref. 10). The axial-velocity component is varied so that the total kinetic energy of the main beam is conserved.

The ion-flux fractions in Table 1 are defined by the second of Eq. (5). "Effective" refers to a value that has been corrected to account for the presence of multiply ionized species. For example,

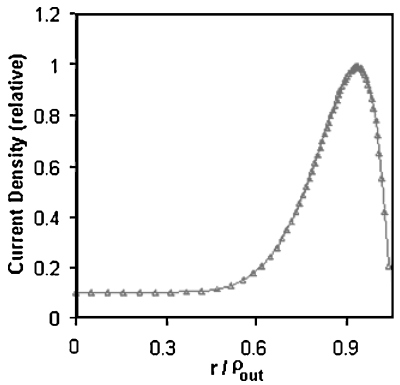

Fig. 4 Nondimensional current-density profile specified at the thruster orifice for the plume calculations.

Table 1 Thruster parameters used in the plume simulations

Model	Parameter	Value
Thruster geometry	Outer radius	0.07 m
	Inner radius	0.05 m
	Neutralizer distance from centerline (CL)	0.1 m
Operating conditions and performance	Anode flow rate	1.07×10^{-5} kg/s
	Neutralizer flow rate	1.02×10^{-6} kg/s
	Thrust	0.208 N
	Propellant utilization	0.9
	Specific impulse	1985 s
	Ion-flux fractions	$f^+ = 0.936$, $f^{2+} = 0.043$, $f^{3+} = 0.021$
	Effective ion-beam speed	2.094×10^4 m/s
	Effective ion current	7.261 A
Neutral gas	Avg. speed from thruster	167 m/s
	Avg. speed from neutralizer	180 m/s
	Background particle density	Based on different values of chamber pressure

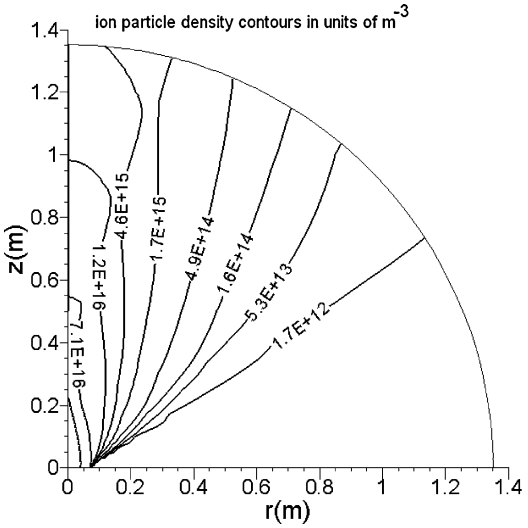

Fig. 5 Computed ion-particle density in the main beam of the BPT-4000 engine.

effective ion current in Table 1 is defined in the first of Eq. (5). The effective beam current is in fact the value used in the calculation of the main beam, because the numerical model assumes the presence of singly ionized particles only. The ion trajectories are computed by assuming that ions of different charge states follow the same trajectories. The computed particle-density profile of the main-beam ions is shown in Fig. 5. Because the numerical technique uses the actual ion trajectories to form the primary grid on which ion densities are computed, finite values of density exist only in regions where ion trajectories have been computed. Thus the main-beam ion density in Fig. 5 does not decrease smoothly as a function of angle beyond the last few ion trajectories:

$$J_{b,\text{eff}} \equiv eAn_e u_b^+ = \frac{e}{m_i}\dot{m}_i \sum_z \sqrt{Z} f^{z+}$$

$$f^{z+} \equiv \frac{n_b^{z+} u_b^{z+}}{\sum_z n_b^{z+} u_b^{z+}} = \frac{\sqrt{Z} n_b^{z+}}{\sum_z \sqrt{Z} n_b^{z+}} \tag{5}$$

The neutral-gas density in a laboratory vacuum chamber consists mainly of three components: un-ionized particles expelled from the thruster, un-ionized neutralizer gas (from the hollow cathode), and background particles. The expansion of neutrals from the thruster is determined using an annular-anode gas-flow model with isotropic emission from the ring. Emission from two disks is computed, one large and one smaller, and the smaller is subtracted from the larger. The density dropoff with r and z from a disk emitting a Maxwellian is calculated using an approximate view factor.[1] Energetic CEX neutrals are negligible compared to the total neutral density and are therefore not included in the model. The hollow-cathode neutrals are assumed to have isotropic emission at a constant temperature equal to the cathode orifice temperature (538°C was taken as the assumed value for the BPT-4000). As also shown in Table 1, the neutralizer is offset from the thruster by 0.1 m from the axis of symmetry. The sum of emitted neutrals from the thruster and hollow cathode is shown in Fig. 6, plotted in logarithmic scale. It will be shown that the precise two-dimensional distribution of neutrals downstream of the thruster exit is not as critical in the comparisons with BPT-4000 laboratory measurements due to the significant contribution of chamber (background) neutrals in the elastic scattering of beam ions. For flight applications, however, the profiles of both the main ion beam and thruster neutrals (including those expelled from the neutralizer) will almost solely determine the populations of scattered ions downstream of the thruster. Therefore, accurate models of neutral particles expelled from the thruster are crucial.

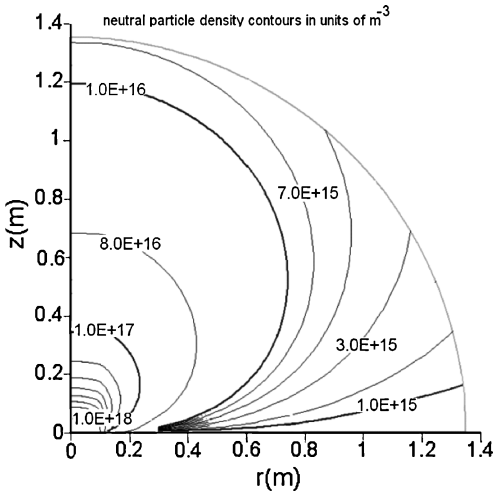

Fig. 6 Specified neutral-particle density profile from thruster and neutralizer.

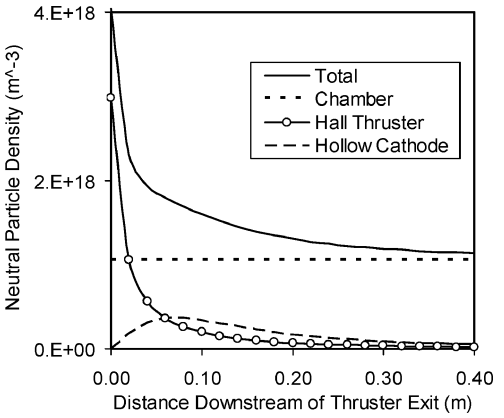

Fig. 7 Neutral-particle density profile along the thruster axis of symmetry.

The chamber background density is assumed to be uniform. Based on values of the ambient temperature (taken to be 300 K) and pressure the background density is determined assuming an ideal-gas law. The value of background pressure used in the plume calculations was taken to be 3.0×10^{-5} torr, and is higher than the measured value by about a factor of 3, but is consistent with integrated current and performance measurements. It is noted that the measured values were obtained using ionization gauges placed at each end of the chamber (upstream and downstream of the thruster), close to the reentrant cryopumps.[6] At 3×10^{-5} torr the corresponding neutral-particle density is approximately 10^{18} m^{-3}. The computed components of neutral-particle density along the thruster centerline are depicted in Fig. 7 as a function of distance from the thruster exit.

Ion–Neutral Elastic Scattering

Differential Cross Section

To compute the flux and energy of scattered ions at any given point in space the differential cross section must first be determined. Referring to Fig. 8, in the classical approach the differential cross section associated with an atomic collision can be calculated from the deflection angle $\Theta(\beta, E_{c,})$ (Ref. 11),

$$\Theta(\beta, E_c) = \pi - 2\beta \int_{R_m}^{\infty} \frac{\mathrm{d}R}{r^2 \sqrt{1 - (\beta/R)^2 - [V(R)/E_c]}} \tag{6}$$

The classical turning point is the largest root of the equation.

$$R = R_m \rightarrow 1 - \beta/R^2 - V(R)/E_c = 0 \tag{7}$$

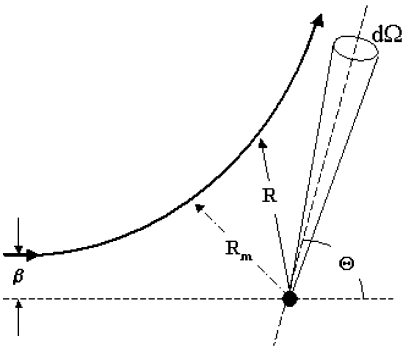

Fig. 8 Classical scattering trajectory.

The deflection angle is computed directly in the elastic-scattering algorithm. Since it is impossible to distinguish between positive and negative deflections in the laboratory when the scattering intensity is measured at a given angle, the scattering angle in the center-of-mass frame, θ, is given by

$$\theta = |\Theta|, \qquad 0 < \theta < \pi \tag{8}$$

The elastic differential cross section is obtained from the equation

$$I_c(\theta, E_c) \equiv \frac{\partial \sigma}{\partial \Omega_c} = \left| \frac{\beta}{(\mathrm{d}\theta/\mathrm{d}\beta)\sin\theta} \right| \tag{9}$$

The differential cross section for ions in an ion–neutral pair [$Xe^+ + Xe$] is calculated as follows:

$$I(\theta, E_c) = \tfrac{1}{2} I_c(\theta, E_c) + \tfrac{1}{2} I_c(\pi - \theta, E_c) \tag{10}$$

Given the angle and energy for each scattering pair (s-point to f-node, as shown in the next section), the impact parameter is obtained by solving Eq. (6) using a Newton–Raphson method. The solution requires a priori knowledge of the interatomic potential function, $V(R)$, which may in general have both attractive and repulsive contributions. The attractive part may lead to a singularity in the differential cross section. The singularity corresponds to a minimum in the deflection angle (leading to the so-called *rainbow* angle). At the high energies of interest in the present work (>300 eV) the deflection-angle function barely exhibits a minimum, because the scattering is governed almost solely by the repulsive part of the interaction potential. In such cases the classical approach (vs the more rigorous quantum-mechanical approach[12]) is sufficiently accurate. Only the repulsive part of the potential function,

$$V(R) = \alpha(\lambda/R)^{\zeta} \tag{11}$$

is included in the thruster plume model. The coefficients that define the functional form of $V(R)$ have been derived from averaged potentials by Amarouche et al. (see Ref. 11) and are also tabulated by Gardner et al.[9] for both positive and negative interaction potentials. The coefficients in Eq. (11) are as follows: $\alpha = 27.21$ eV, $\lambda = 2.11$ Å, and $\zeta = 6.57$. The derivative in Eq. (9) is obtained using a first-order forward finite difference.

In the case of equal masses and a stationary target particle the deflection angles and energies in the laboratory and center-of-mass (CM) frames are simply related by (see also Appendix)

$$\vartheta = \theta/2, \qquad E_L = 2E_c \tag{12}$$

Using the angle relation in Eq. (12) it can be shown (see Appendix) that the CM differential cross sections may be converted into the laboratory frame of reference using the equation

$$I_L \equiv \frac{\partial \sigma}{\partial \Omega_L} = \frac{\partial \sigma}{\partial \Omega_c} 4\cos\vartheta \tag{13}$$

Although the differential cross section decreases with increasing impact energy, the reduction is not directly proportional to the increase in energy. Figure 9 plots the ratio of the total differential cross

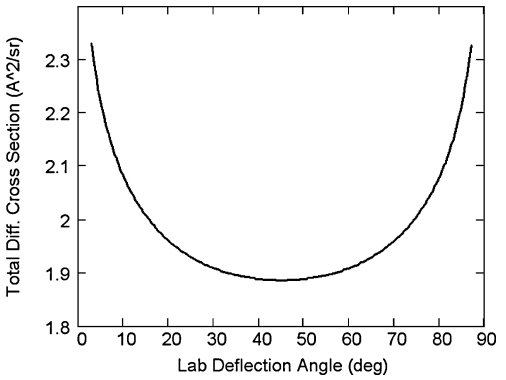

Fig. 9 Classical differential cross section as a function of angle in the lab frame for the Xe + Xe^+ elastic scattering pair at $E_{c,L} = 300$ and 3000 eV.

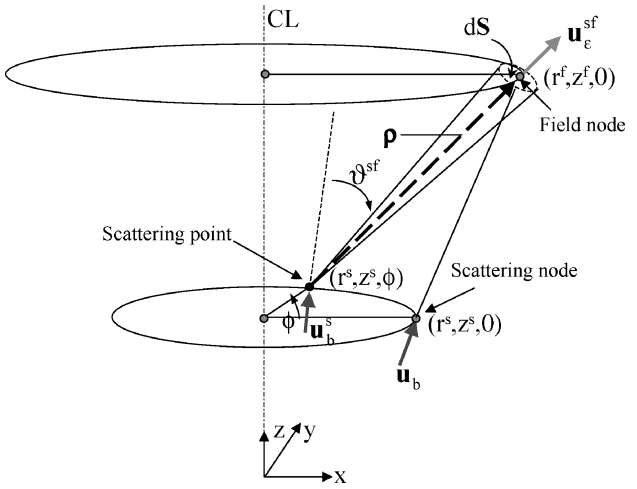

Fig. 10 Geometry used in the formulation of the elastic-scattering algorithm.

section $I(\vartheta, E_L)$ for $E_L = 300$ eV over $I(\vartheta, E_L)$ for $E_L = 3000$ eV. At $\pi/2$, for example, an order-of-magnitude increase in energy reduces the differential cross section (intensity of scattering per unit solid angle) by a factor of only about 1.9. Thus as the jet power and specific impulse are increased in propulsion systems such as ion and Hall engines, the erosion rate of the surrounding critical surfaces on the spacecraft due to the impact of elastically scattered ions will continue to increase.[13]

Particle Density, Average Velocity, and Average Energy of the Elastically Scattered Ions

To formulate the elastic-scattering model we refer to the schematic in Fig. 10. It is assumed that at the scattering point "s," one scattering event occurs as the main-beam ion flux, $\boldsymbol{F}_b^s = n_b^s \boldsymbol{u}_b^s$, impacts one stationary neutral particle. Once scattered, an ion does not undergo another collision. Then the particle flow rate $\mathrm{d}N_\varepsilon/\mathrm{d}t$ through the incremental surface $\mathrm{d}S = \rho^2 \mathrm{d}\Omega$ is given by

$$\frac{\mathrm{d}N_\varepsilon}{\mathrm{d}t} = F_b^s I \frac{\mathrm{d}S}{\rho^2} \tag{14}$$

The particle flow rate is also equal to

$$\frac{\mathrm{d}N_\varepsilon}{\mathrm{d}t} = n_\varepsilon^{\mathrm{sf}} u_\varepsilon^{\mathrm{sf}} \mathrm{d}S \tag{15}$$

Combining Eqs. (13), (14), and (15) yields

$$F_\varepsilon^{\mathrm{sf}} = n_\varepsilon^{\mathrm{sf}} u_\varepsilon^{\mathrm{sf}} = 4 F_b^s I \cos\vartheta^{\mathrm{sf}} \big/ \rho^2 \tag{16}$$

Equation (16) expresses the magnitude of the flux vector $F_\varepsilon^{\mathrm{sf}} = |\boldsymbol{F}_\varepsilon^{\mathrm{sf}}|$ at the field-node location $(r^f, z^f, 0)$ due to scattering of the main-beam flux by a neutral at the scattering point (r^s, z^s, ϕ).

It is also assumed that the distance between nodes is much larger than interatomic distances. Thus, the scattering event is treated as an elastic collision. Because both momentum and kinetic energy are conserved in the scattering event,

$$u_\varepsilon^{\mathrm{sf}^2} = u_b^{s^2} \cos^2 \vartheta^{\mathrm{sf}} \tag{17}$$

which also yields the density of scattered ions at f as follows:

$$n_\varepsilon^{\mathrm{sf}} = \frac{F_\varepsilon^{\mathrm{sf}}}{u_\varepsilon^{\mathrm{sf}}} = \frac{4n_b^s u_b^s I \cos \vartheta^{\mathrm{sf}}}{\rho^2 u_b^s \cos \vartheta^{\mathrm{sf}}} = \frac{4n_b^s I}{\rho^2} \tag{18}$$

The contributions to f from all points along the scattering ring defined by each scattering node at $(r^s, z^s, 0)$ and by all nodes are summed as shown in Eq. (19):

$$n_\varepsilon(r, z) = \int_\upsilon \frac{4n_b^s I}{\rho^2} n_0^s \, \mathrm{d}\upsilon = 4 \iint r^s \mathrm{d}r^s \mathrm{d}z^s \times 2 \int_0^\pi n_b^s(r^s, z^s) n_0^s(r^s, z^s) \frac{I(r^s, z^s, \phi)}{\rho(r^s, z^s, \phi)^2} \, \mathrm{d}\phi \tag{19}$$

The integral in Eq. (19) is determined numerically. It is noted that $2\pi \iint r^s \mathrm{d}r^s \mathrm{d}z^s$ is the volume associated with node s, which our finite element code has already calculated as the sum of the integrated weights of node s in the surrounding elements. Thus, only the angular integral need be calculated anew for each source point/field point pair.

The two components of the flux vector are determined by

$$Fr_\varepsilon^{\mathrm{sf}} = \left|\boldsymbol{F}_\varepsilon^{\mathrm{sf}}\right| [(r^f - r^s \cos\phi)/|\rho|], \qquad Fz_\varepsilon^{\mathrm{sf}} = \left|\boldsymbol{F}_\varepsilon^{\mathrm{sf}}\right| [(z^f - z^s)/|\rho|] \tag{20}$$

and are combined with eq. (18) to compute the average velocity components of the scattered ions as follows:

$$ur_\varepsilon(r, z) = \frac{\int_\upsilon Fr_\varepsilon^{\mathrm{sf}} n_0 \, \mathrm{d}\upsilon}{n_\varepsilon(r, z)}, \qquad uz_\varepsilon(r, z) = \frac{\int_\upsilon Fz_\varepsilon^{\mathrm{sf}} n_0 \, \mathrm{d}\upsilon}{n_\varepsilon(r, z)} \tag{21}$$

As with Eq. (19), the integrals in Eq. (21) are determined numerically. Referring to Fig. 10, it is noted that

$$\rho^2 = (r^f - r^s \cos\phi)^2 + (-r^s \sin\phi)^2 + (z^f - z^s)^2 \tag{22}$$

$$\cos \vartheta^{\mathrm{sf}} = \frac{ur_b \cos\phi (r^f - r^s \cos\phi) + ur_b \sin\phi (-r^s \sin\phi) + uz_b (z^f - z^s)}{|\boldsymbol{u}_b||\boldsymbol{\rho}|}$$

$$\frac{\pi}{2} > \vartheta \geq 0 \tag{23}$$

Finally, the average energy of the scattered ions at each field node is computed using the energy flux and the particle flux as shown in the equation

$$\bar{\in}_\varepsilon(r, z) = \frac{\int_V F_\varepsilon^{\mathrm{sf}} \in_\varepsilon^{\mathrm{sf}} n_0 \, \mathrm{d}V}{\int_V F_\varepsilon^{\mathrm{sf}} n_0 \, \mathrm{d}V} \tag{24}$$

where

$$\in_\varepsilon^{\mathrm{sf}} = \tfrac{1}{2} m_i u_\varepsilon^{\mathrm{sf}^2} \tag{25}$$

It is interesting to note here that the general classical scattering formulation outlined above is ideally not exclusive of what is commonly termed "resonant charge-exchange" scattering. Indeed, if the impact parameter β is large enough the ion will simply exchange an electron with the neutral, and the differential cross section integrated over all solid angles Ω would approximately equal the total cross section for CEX, provided that the interaction-potential function $V(R)$ accurately captured the force field between the colliding particles at large distances. In the present calculations we refer to elastically scattered ions when the associated ion energies are above 20 eV, which is only an approximation that is based on the observations illustrated in Fig. 2.

Comparison with Measurements

Results from the plume calculations using the elastic-scattering cross-sectional treatments described above are compared with RPA measurements. To draw conclusions specifically about the elastic-scattering ion-production source, comparisons are performed using a reduced set of RPA data. Specifically, the high-energy part of the energy spectrum associated with the main-beam ions was removed by fitting a smooth curve to the higher-energy data points and subtracting it from the total ion current, as shown in Fig. 11. (The difference between the two profiles is the elastically scattered ion component.) The average energy of the main-beam ions, E_L, is found to be 273 eV. The computed particle density of the elastically scattered ions is depicted in Fig. 12. In Fig. 13 the results from the elastic scattering calculation for $\bar{\in}_\varepsilon(\psi)/E_L$ at $P = 0$ and 3.0×10^{-5} torr are compared with the data taken 1 m away from the thruster exit. It is noted that the values at 55 and 65 deg in Fig. 13 are rough estimates from broad peaks (Fig. 2). Also shown for comparison in Fig. 13 is the square of $\cos(\psi)$. The comparison shows that the maximum error for the nominal case of $P = 3 \times 10^{-5}$ torr is approximately 20% (at 25 deg), which may be due to the flux averaging that has been used to determine the average ion energy [Eq. (24)]. The error from this averaging would tend to increase with increasing energies. Another source of error may be the assumption of uniform background density, whose validity diminishes close to the thruster (where most of the scattering occurs). For contrast, the case with no background pressure is also plotted in Fig. 13.

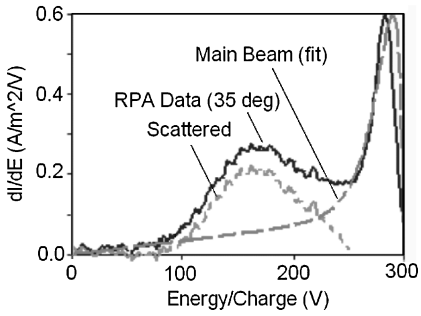

Fig. 11 RPA data at 35 deg from the thruster axis with fit of main-beam ion energy only.

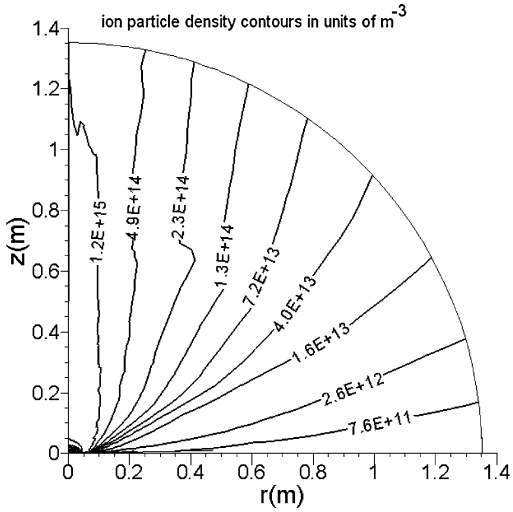

Fig. 12 Computed elastically scattered ion-particle density in the plume of the BPT-4000 engine operating in the laboratory ($P = 3.3 \times 10^{-5}$ torr).

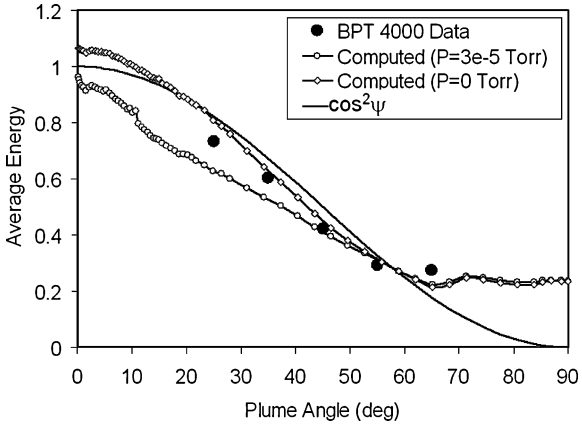

Fig. 13 Comparisons between computed energy of elastically scattered ions $\bar{\in}_{\varepsilon}(\psi)$ and measurements in the plume of the BPT-4000 engine operating in the laboratory.

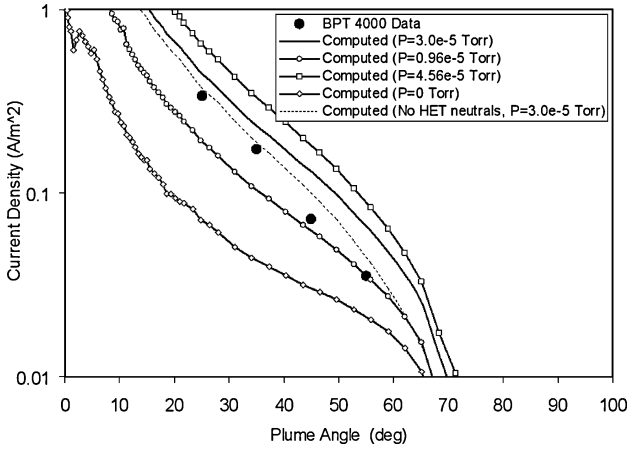

Fig. 14 Comparisons between computed flux of elastically scattered ions for three chamber pressures and measurements in the plume of the BPT-4000 engine.

The significance of accurate neutral-particle profiles is more evident through the current-density comparisons in Fig. 14. It is shown that the computed flux of scattered ions for the 3×10^{-5} torr case, 1 m from the thruster exit, is within a factor of 2 of the measured value, with the discrepancy being higher at the larger angles. Also shown in Fig. 14 are the values computed using the maximum and minimum pressures that had been measured during the experiments. The case of zero background pressure is also plotted. At a lower pressure, for example at $\sim 1 \times 10^{-5}$ torr, the comparison is better at the larger angles but is about a factor of 2 lower than the measured value at the smaller angles. The comparisons suggest that to improve our predictive capability for the scattered ion populations in the laboratory a better model of the background neutrals would be needed. At 3.0×10^{-5} torr, when no thruster neutrals are included in the calculation, the comparison with the data seems to improve, which may be fortuitous, because un-ionized particles are indeed expelled from the thruster. It is, however, possible that the concentration of these thruster neutrals at the exit, which was determined using only average thruster operating values and assumed neutral-particle speeds (Table 1), has been overestimated. Finally, it is noted that the computed values in Fig. 14 have not accounted for the reduction of the elastically scattered ion flux due to charge-exchange collisions, and are therefore an upper-bound estimate. Previous calculations assumed that as much as 60% of the total ion flux reaching the detector was lost by charge-exchange scattering.[9] The estimate was based on the ratio of the beam current at the exit plane to the current measured by the RPA, 1 m away from the thruster exit. Based on the performance parameters of Table 1 the former was approximated as ~7.3 A while the latter was measured as 4.7 A (Ref. 9). Also not included is the depletion of the main-beam ions by CEX collisions, which should introduce negligible error, because the CEX ion densities are in general at least one to two orders of magnitude less than the main-beam ion densities.

As expected, the comparisons with the data illustrate the importance of accurate determination of neutral-particle concentrations in any theoretical effort to predict the flux and energy of the elastically scattered ions. In this effort the exact value of the background density near the thruster exit is unknown because the pressure probes are placed far from the thruster. Moreover, background neutral particles in the laboratory consist of atoms and molecular constituents other than xenon. Consequently, the interaction potentials and in turn the differential cross sections associated with the scattering of xenon main-beam ions and background particles may differ considerably from the ones computed herein. Of course, for space-flight applications the determination of laboratory-induced contributions to elastic scattering is relevant only as a means of preventing laboratory effects from distorting any predictions of the thruster effluents during flight.

Conclusions

A plume model has been developed to elucidate experimental observations of secondary high-energy peaks in the plume of a 4-kW class Hall-effect thruster. In the model, the main-beam expansion is calculated using a fluid technique in which ion trajectories serve as streamlines. The differential cross sections associated with the ion–neutral scattering are computed classically in the model. Both the computed intensity and the energy dependence of the scattering peaks have been compared with measurements. The relatively good agreement with measured values of the energy at plume angles greater than 25 deg exposes the importance of elastic scattering as a source of highly energetic ions. Although these ions account for only a few percent of the main beam density, they are found to be the principal ion component with energies exceeding 100 eV at angles higher than 45 deg with respect to the thruster axis. At such high energies these large-angle scattered ions pose a concern for a variety of spacecraft-surface-interaction issues (e.g., erosion from sputtering). The comparisons between model results and measurements also emphasize the importance of accurate predictions of neutral-particle concentrations as well as collision cross sections associated with the scattering species.

Appendix: Frame Transformation

The most general elastic-collision process between two particles of unequal masses m_1 and m_2, velocity vectors before the collision $\boldsymbol{u}_1$ and $\boldsymbol{u}_2$, and velocity vectors after the collision $\boldsymbol{u}'_1$ and $\boldsymbol{u}'_2$, can be represented by the geometrical construction in Fig. A1 (top) using the following definitions:

1) Relative velocities: $\boldsymbol{U} = \boldsymbol{u}_1 - \boldsymbol{u}_2$, $\boldsymbol{U}' = \boldsymbol{u}'_1 - \boldsymbol{u}'_2$
2) Center-of-mass velocity: $\boldsymbol{u}_c = (m_1\boldsymbol{u}_1 + m_2\boldsymbol{u}_2)/(m_1 + m_2)$
3) Reduced mass: $M = m_1 m_2/(m_1 + m_2)$

In the case of equal masses $m_1 = m_2 = m$ and one stationary particle, $\boldsymbol{u}_2 = 0$, the geometric construction reduces to the illustration in Fig. A1 (bottom). It can then easily be seen that

$$2\vartheta + (\pi - \theta) = \pi \Rightarrow 2\vartheta = \theta \tag{A1}$$

Also, the initial kinetic energy of the relative motion (center-of-mass system) is given by the equation

$$E_c = \tfrac{1}{2} M U^2 \tag{A2}$$

It then follows that in the purely elastic collision,

$$E_c = \tfrac{1}{2}(m/2)u_1^2 \Rightarrow E_c = E_1/2,\ E_1 \equiv \tfrac{1}{2} m_1 u_1^2 \tag{A3}$$

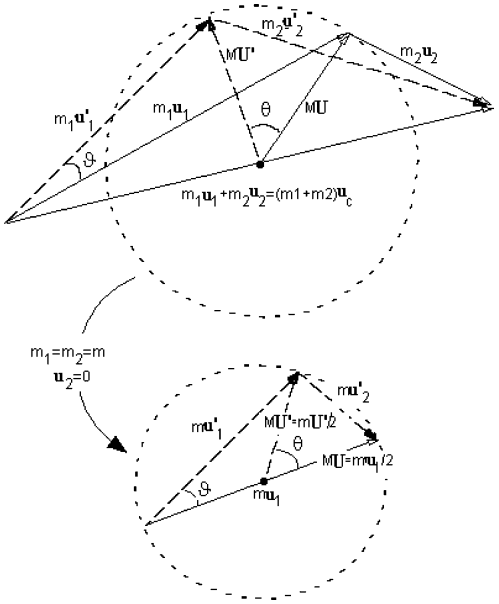

Fig. A1 Geometrical construction of the general elastic-collision process (top) reduced to a simplified construction for equal masses and one stationary particle (bottom).

The center-of-mass differential cross sections can then be converted into the laboratory frame of reference as follows:

$$\frac{\partial\sigma}{\partial\Omega_L} = \frac{\partial\sigma}{\partial\Omega_c}\frac{\partial\Omega_c}{\partial\Omega_L}$$

$$= \frac{\partial\sigma}{\partial\Omega_c}\frac{\sin\theta\,\mathrm{d}\theta}{\sin\vartheta\,\mathrm{d}\vartheta}$$

$$= \frac{\partial\sigma}{\partial\Omega_c}\frac{\sin(2\vartheta)2\mathrm{d}\vartheta}{\sin\vartheta\,\mathrm{d}\vartheta}$$

$$\Rightarrow \frac{\partial\sigma}{\partial\Omega_L} = \frac{\partial\sigma}{\partial\Omega_c}4\cos\vartheta \tag{A4}$$

Acknowledgments

The authors acknowledge Rainer Dressler of the Air Force Research Laboratory and Iain Boyd of the University of Michigan for their insightful contributions to the determination of the scattering cross sections. The authors are also grateful to James Pollard of the Aerospace Corporation for providing excellent experimental measurements of the Hall thruster plume.

References

[1]Mikellides, I. G., Jongeward, G. A., Katz, I., and Manzella, D. M., "Plume Modeling of Stationary Plasma Thrusters and Interactions with the Express-A Spacecraft," *Journal of Spacecraft and Rockets*, Vol. 39, No. 6, 2002, pp. 894–903.

[2]Davis, V. A., et al., "Ion Engine Generated Charge Exchange Environment: Comparison Between NSTAR Flight Data and Numerical Simulations," AIAA Paper 2000-3529, July 2000.

[3]Samanta Roy, R. I., Hastings, D. E., and Gatsonis, N. A., "Numerical Study of Spacecraft Contamination and Interactions by Ion-Thruster Effluents," *Journal of Spacecraft and Rockets*, Vol. 33, No. 4, 1996, pp. 535–542.

[4]VanGilder, D. B., Boyd, I. D., and Keidar, M., "Particle Simulations of a Hall Thruster Plume," *Journal of Spacecraft and Rockets*, Vol. 37, No. 1, 2000, pp. 129–136.

[5]Pullins, S., Dressler, R. A., Chiu, Y., and Levandier, D. J., "Ion Dynamics in Hall Effect and Ion Thrusters: $Xe^+ + Xe$ Symmetric Charge Transfer," AIAA Paper 00-0603, Jan. 2000.

[6]Pollard, J. E., et al., "Ion Flux, Energy, Charge-State Measurements for the BPT-4000 Hall Thruster," AIAA Paper 01-3351, July 2001.

[7]Birdsall, C. K., and Langdon, A. B., "Why Attempting to Do Plasma Physics via Computer Simulation Using Particles Makes Good Physical Sense," *Plasma Physics via Computer Simulation*, McGraw–Hill, New York, 1985, Chap. 1, pp. 3–6.

[8]Mikellides, I. G., Kuharski, R. A., Mandell, M. J., Gardner, B. M., "Assessment of Spacecraft Systems Integration Using the Electric Propulsion Interactions Code (EPIC)," AIAA Paper 2002-3667, July 2002.

[9]Gardner, B. M., Katz, I., Davis, A., and Mandell, M., "Hall Current Thruster (HCT) IR&D Plume Environment Characterization and Electrostatic Return Current Assessment," Final Rept. for Lockheed Martin Space Systems Co. MTSD-DPR-01-16648, San Diego, CA, Jan. 2001.

[10]Pollard, J. E., and Beiting, E. J., "Ion Energy, Ion Velocity, and Thrust Vector Measurements with the SPT-140 Hall Thruster," *Proceedings of the 3rd International Conference on Spacecraft Propulsion*, ESA-SP-365, Cannes, France, Oct. 2000, pp. 789–796.

[11]Child, M., "Classical Scattering by a Central Force," *Molecular Collision Theory*, Academic Press, London, 1974, Chap. 2, pp. 9–26.

[12]Mott, N. F., and Massey, H. S. W., *The Theory of Atomic Collisions*, Clarendon, Oxford, 1949, Chap. 1, 5, and 12, pp. 1–15, 19–41, and 266–294.

[13]Mikellides, I. G., Mandell, M. J., Kuharski, R. A., Davis, D. A., Gardner, B. M., and Minor, J., "The Electric Propulsion Interactions Code (EPIC): A Member of the NASA Space Environment and Effects Program (SEE) Toolset," AIAA Paper 2003-4871, July 2003.